Catalysis Today 437 (2024) 114763

Contents lists available at ScienceDirect

Catalysis Today

journal homepage: www.elsevier.com/locate/cattod

Synthesis of graphene mesosponge using CaO nanoparticles formed from $CaCO_3$

Shogo Sunahiro [a], Kritin Pirabul [b], Zhengze Pan [c], Takeharu Yoshii [b], Yuichiro Hayasaka [d], Qi Zhao [e], Rachel Crespo-Otero [e], Devis Di Tommaso [e,f], Takashi Kyotani [b], Hirotomo Nishihara [b,c,*]

[a] R & D Strategy Division, Tokai Carbon Co., Ltd., Aoyama Building, 1-2-3 Kita Aoyama, Minato-ku, Tokyo 107-8636, Japan
[b] Institute of Multidisciplinary Research for Advance Materials, Tohoku University, 2-1-1 Katahira, Aoba-ku, Sendai, Miyagi 980-8577, Japan
[c] Advanced Institute for Materials Research (WPI-AIMR), Tohoku University, 2-1-1 Katahira, Aoba-ku, Sendai, Miyagi 980-8577, Japan
[d] The Electron Microscopy Centre, Tohoku University, 2-1-1 Katahira, Aoba, Sendai, Miyagi 980-8577, Japan
[e] School of Physical and Chemical Sciences, Queen Mary University of London, Mile End Road, London E1 4NS, UK
[f] Digital Environment Research Institute, Queen Mary University of London, Empire House, 67-75 New Road, London E1 1HH, UK

ARTICLE INFO

Keywords:
Mesoporous carbons
Three-dimensional graphene
Catalytic methane decomposition
Template
Base sites

ABSTRACT

While graphene mesosponge (GMS) is a new type of mesoporous material with the potential for a variety of applications, its synthesis process requires costly templates such as Al_2O_3 and MgO nanoparticles. In this study, we present a new synthesis method for GMS, which achieves a high specific surface area of 1720 $m^2\ g^{-1}$ by employing calcium oxide (CaO) nanoparticles as templates. The CaO nanoparticles with an approximate diameter of 86 nm are formed through the thermal decomposition of calcium carbonate nanoparticles. However, the calcium carbonate nanoparticles contain a small amount of Mg (2 wt %), and the thermal decomposition process also yields impurities, including Mg. When the CaO nanoparticles, including the Mg-based impurities, are subjected to chemical vapor deposition, the CaO surface can be coated with a thin carbon layer, primarily consisting of single-layer graphene through the specific catalysis of the CaO surface in facilitating the CH_4-to-C conversion reactions. However, at the same time, the presence of Mg-based impurities leads to the formation of low-crystalline carbons, which have a detrimental effect on the subsequent high-temperature annealing at 1800 °C, following the template removal process, resulting in an excessive number of edge sits in the GMS. We have found that the harmful low-crystalline carbons can be eliminated through heat treatment in air at 350 °C. By adopting such a removal process, high-quality GMS with a minimal number of edge sites can be produced.

1. Introduction

Carbon-based materials have been widely used for many applications due to the advantages of their light weight, mechanical strength, chemical and thermal stability, and electric conductivity. [1,2] Their properties greatly vary depending on their nanostructures, *i.e.*, the structures and arrangement of the primal structure unit, graphene. Regarding the nanoporous carbons, not only the rational design of porous structures but also the precise control of the carbon framework is crucial to exhibiting desirable properties and performance. A traditional activation process cannot precisely control fine nanostructures such as pore-size distribution, graphene stacking number, and chemical forms of carbon edge sites. [3] To overcome the limitation in nanostructure controllability, a variety of new approaches have been proposed, for example, sol-gel synthesis, [4,5] template carbonization, [6–9] exfoliation of graphite, [10,11] and direct conversion of porous organic substances. [12–14] Template carbonization especially has a long history, pioneered by the SiO_2-templated carbon in 1982 [15] and NaCl-templated carbon in 1987.[16] Kyotani *et al.* further extended this methodology to 1-dimensional, [17] 2-dimensional, [18] and 3-dimensional nanostructured carbons. [19] The use of 3-dimensional templates especially has greatly expanded the range of synthesis possibilities for porous carbon materials. Zakhidov *et al.* have used silica opals as hard templates to synthesize carbon inverse opals with ordered

* Corresponding author at: Institute of Multidisciplinary Research for Advance Materials, Tohoku University, 2-1-1 Katahira, Aoba-ku, Sendai, Miyagi 980-8577, Japan.
E-mail address: hirotomo.nishihara.b1@tohoku.ac.jp (H. Nishihara).

https://doi.org/10.1016/j.cattod.2024.114763
Received 1 March 2024; Received in revised form 21 April 2024; Accepted 24 April 2024
Available online 26 April 2024

macropores. [20] Ryoo's group and Hyeon's group independently developed methods for synthesizing ordered mesoporous carbons using mesoporous silicas as hard templates. [21,22] Not only hard templates but also soft templates have been developed to synthesize porous carbon materials with ordered porous structures. Ling *et al.* successfully synthesized ordered mesoporous carbons through the carbonization of block copolymers, which had mesoscopic structures formed by microphase separation. [23] Nishiyama's group [24] and Meng's group [25] have independently produced ordered mesoporous carbons using surfactant micelles as soft templates. While the controllability of carbon pores has been remarkably improved by the template-carbonization techniques, controlling the chemical structure of pore walls, particularly the number of graphene layers and the number of edge sites, remains a challenging target. In 2016, our group developed a new class of material, graphene mesosponge (GMS), based on template carbonization using γ-alumina (γ-Al_2O_3) nanoparticles as templates. [26] GMS is single-walled nanoporous graphene that is almost free from carbon edge sites, overcoming the long-standing challenge of achieving high porosity and edge-free structure. While conventional porous carbon materials with a high specific surface area inevitably contain a significant number of carbon edge sites, GMS manages to combine high porosity with a structure devoid of edges. With its developed mesoporosity, high surface area, high electric conductivity, excellent durability, and mechanical flexibility, GMS is expected to be used in many applications, such as new types of sorbent, durable catalyst support, [27] high-voltage supercapacitors, [28] cathodes for lithium-air batteries, [29–31] and a new type of heat pumps. [32]

The key process of GMS synthesis is chemical vapor deposition (CVD) of methane (CH_4) on metal oxide, typically γ-Al_2O_3 or magnesium oxide (MgO). It is known that the surface of specific types of metal oxides catalyzes the CVD-based conversion of hydrocarbons into graphene sheets. [33] As for the GMS synthesis, the entire surface of γ-Al_2O_3 or MgO nanoparticles can be uniformly coated with an extremely thin carbon layer, almost corresponding to single-layer graphene, by the unique catalysis of these metal oxides over CVD using CH_4 as a carbon source. [34] By subsequent template removal followed by high-temperature annealing at 1800 °C, GMS with edge-free graphene walls can be obtained. [35] We have examined the detailed mechanisms of the transition-metal-free pyrolytic carbon deposition from CH_4 on γ-Al_2O_3 and MgO through comprehensive research using experimental analysis and quantum mechanical calculations. [34,36] Interestingly, γ-Al_2O_3 and MgO share an intrinsically similar reaction mechanism, although γ-Al_2O_3 and MgO have been known to have different catalytic features of solid acid and base, respectively. When CH_4 contacts γ-Al_2O_3 or MgO at a high temperature, at first, O of the metal oxide is reductively eliminated as CO, and the oxygen vacancy sites are formed. Then, the oxygen vacancy sites catalyze the CH_4-to-C conversion. Moreover, the graphene growth rate of the first layer directly attached to the metal oxide surface is much larger than that of the following stacked layers in both γ-Al_2O_3 and MgO. [34] The preferential growth of the first graphene layer allows for a uniform coating of the entire surface of metal oxides with single-layer graphene, enabling the synthesis of GMS composed of single-layer graphene walls. Towards the industrialization of GMS based on a sustainable process, this work focuses on the production of GMS with developed porosity using calcium oxide (CaO), a solid base similar to MgO, as a further cost-effective template over γ-Al_2O_3 and MgO. Ca is also a ubiquitous element, and CaO can be easily obtained by the thermal decomposition of $CaCO_3$, which is abundant in nature. In this work, we examine the feasibility of $CaCO_3$ nanoparticles, which are mass-produced in the industry with low prices for filler applications. [37]

There have been many reports on the synthesis of porous carbons by a hard-template method using $CaCO_3$ or CaO. One of the major methods is the carbonization of the mixture of $CaCO_3$ and solid carbon sources such as sucrose. [37–39] In this case, however, the resulting materials are composed of disordered carbon frameworks with a large number of edge sites and graphene stacking structures. The challenge is to obtain nanoporous materials with single-layer graphene walls with an edge-free structure. Another method is CVD at 950–1200 °C using as template CaO formed by the thermal decomposition of $CaCO_3$ nanoparticles. [40–43] However, the CVD process has not been precisely controlled due to an unclear reaction mechanism, and the resulting carbon materials have a significant amount of graphene stacking structures. Thus, the maximum specific surface area of the carbon materials is at most 527 $m^2\ g^{-1}$, which is much smaller than the theoretical value of graphene (2627 $m^2\ g^{-1}$). In this work, we carefully examine the CVD conditions of CaO generated by the thermal decomposition of $CaCO_3$ nanoparticles and figure out the optimal CVD conditions that allow uniform coating of the entire surface of CaO with single-layer graphene walls. Then, through graphene zipping reactions, which are graphene-graphene coalescence reactions occurring at temperatures ranging from 900 to 1800 °C, [35] we demonstrate the synthesis of high-quality GMS with a specific surface area of 1720 $m^2\ g^{-1}$ and superior oxidation resistance.

2. Experimental

2.1. Analysis of $CaCO_3$ and CaO

In this work, $CaCO_3$ nanoparticles (denoted SK2), kindly provided by Shiraishi Central Laboratories Co., Ltd., were used as precursors for CaO. SK2 contains approximately 2 wt % magnesium, and its particle size is around 28 nm. The results of elemental analysis are presented in Supporting Information Table S1.

The thermal decomposition process from $CaCO_3$ to CaO was analyzed by gas chromatography (GC; Varian, 490-GC) and thermogravimetry (TG; NETZSCH, STA 2500 Regulus). The detailed heating conditions are described in the captions of the corresponding Fig. 1a and b, respectively. The changes in crystal structure and surface area before and after the heat treatment at 850 °C or 900 °C were evaluated by X-ray diffraction (XRD; Rigaku, MiniFlex600) and N_2 adsorption at —196 °C measured on a volumetric sorption analyzer (BEL Japan, BELSORP MAX), respectively. The Brunauer–Emmett–Teller (BET) method was applied to the N_2 adsorption isotherm in the pressure range of P/P_0 = 0.05–0.30 to estimate the specific surface area (S_{BET}). The base sites of heat-treated CaO were quantified by temperature-programmed desorption of CO_2 (CO_2–TPD). [34] First, $CaCO_3$ was converted into CaO by heating it from roome temperature up to 900 °C in a quartz-tube reactor under He flow. After cooling down to room temperature, the sample was exposed to a mixture of He (99 vol %) and CO_2 (1 vol %) gas for 30 min to adsorb CO_2 onto the base sites. Subsequently, the sample was heated to 900 °C at a heating rate of 5 °C min^{-1} under He flow, and the CO_2 desorption was quantified by GC. Also, the acid sites of CaO heat-treated at 900 °C were quantified using the NH_3-TPD technique, similar to the CO_2-TPD method, except that the adsorption temperature for NH_3 was 100 °C. [34]

2.2. Analysis of the reaction of methane on CaO

During the CVD, GC was used to analyze the initial reaction between CaO and methane (CVD-GC). Approximately 1 g of $CaCO_3$ was placed in a tube furnace connected to the gas chromatograph, and the sample was heated to 900 °C at a heating rate of 10 °C min^{-1} under He flow to convert the $CaCO_3$ into CaO. To reduce the pressure drop, quartz sand was mixed with the $CaCO_3$ prior to heating. It was confirmed beforehand that the quartz sand acted as an inert background throughout the measurement. When CO_2 and H_2O emissions from the CaO, generated from $CaCO_3$, became negligible at 900 °C, the He flow was switched to a mixture of He (99 vol %) and CH_4 (1 vol %), and the reaction between CaO and methane was analyzed. Due to the upper detection limit of CH_4, a smaller CH_4 concentration (1 vol %) than GMS synthesis (20 vol %) was used. CH_4 was supplied from a highly-purity CH_4 cylinder (99.99 %)

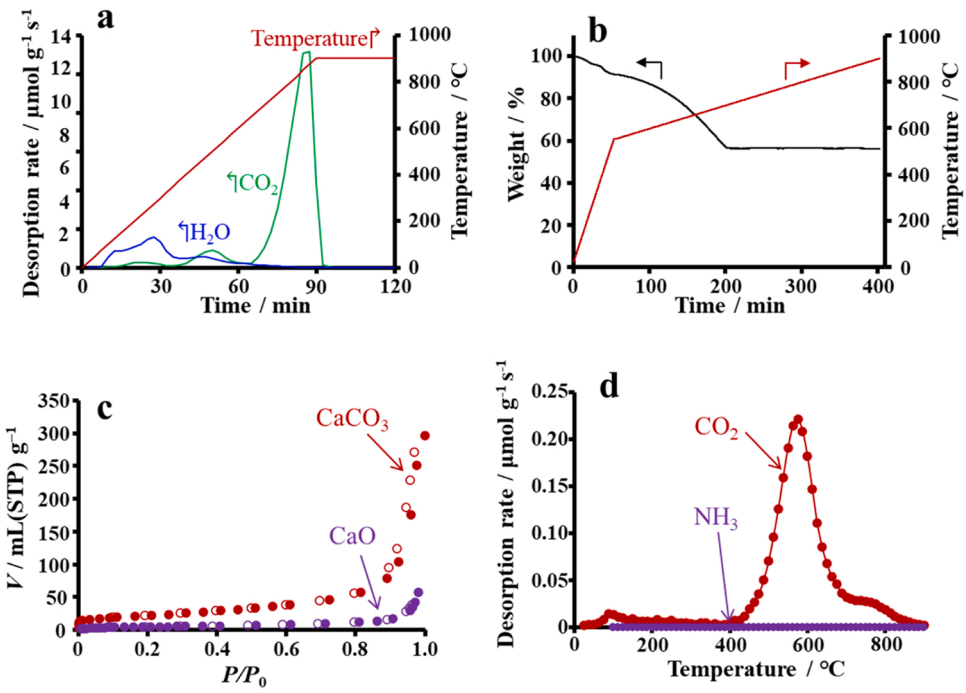

Fig. 1. (a) GC profiles of CO_2 and H_2O emitted from $CaCO_3$ in He. The heating rate is 10 °C min^{-1}. (b) TG curves of $CaCO_3$ in Ar. The heating rate is 10 °C min^{-1} up to 550 °C and 1 °C min^{-1} from 550 °C to 900 °C. (c) N_2 adsorption-desorption isotherms of $CaCO_3$ before and after the heat treatment at 900 °C. After the heat treatment, $CaCO_3$ is converted into CaO. (d) The profiles of CO_2-TPD and NH_3-TPD on CaO formed by the decomposition of $CaCO_3$ at 900 °C.

through a molecular sieve filter to reduce the amount of CO_2, which is inevitably contained as an impurity, down to a negligible level (76 ppm). The gas emission behavior on CaO was compared with those on MgO (US Research Nanomaterials, average particle size is 27 nm) and γ-Al_2O_3 (TH80/170, Sasol, average particle size is 11 nm).

2.3. Synthesis of GMS

$CaCO_3$ (2–3 g) was placed in a vertical quartz tube and was heated from room temperature to either 850 °C or 900 °C at a rate of 10 °C min^{-1} in an Ar flow. Once the temperature reached either 850 °C or 900 °C, it was maintained for 30 min for stabilization. Then, the Ar gas was switched to a mixture of Ar+CH_4 (20 vol %), and CVD was performed at the same temperatures for durations specified in Table 1. Afterward, the mixture gas was switched back to Ar, and the sample was allowed to cooled down in Ar. The resulting carbon-coated CaO (C/CaO) was then washed with 5 M HCl at room temperature for 5 h to remove CaO. After thoroughly washing with pure water and then acetone, the sample was dried at 150 °C to obtain carbon mesosponge (CMS). CMS was then annealed at 1800 °C for 1 h in the vacuum to obtain GMS.

Table 1
Summary of CVD conditions (temperature and period) and the properties of CMS.

Entry	Conditions	N_{stack}[a]	Y_{carbon}[b] (%)	S_{BET}[c] (m^2 g^{-1})	$N_{stack\text{-}BET}$[d]	V_{total}[e] (cm^3 g^{-1})
1	900 °C, 2 h	3.1	3.9	1232	2.1	2.3
2	900 °C, 1 h 20 min	2.2	2.8	1438	1.8	2.1
3	900 °C, 40 min	1.8	2.3	1647	1.6	2.2
4	850 °C, 2 h	1.6	2.5	1684	1.6	2.3
5	850 °C, 1 h 20 min	1.4	2.2	1838	1.4	2.4
6	850 °C, 40 min	1.4	2.2	1849	1.4	2.5
7	850 °C, 30 min	1.2	1.9	1475	1.8	2.0

[a] The average stacking number of graphene layers calculated by carbon-loading amount in C/CaO.
[b] Carbon yield.
[c] BET surface area.
[d] The average graphene stacking number of graphene layers calculated by BET surface area of CMS.
[e] Total pore volume calculated from adsorption isotherm at P/P_0 = 0.96.

2.4. Characterization

The carbon-loading (W_{carbon} [g g^{-1}]) onto the CaO nanoparticles via CVD was estimated from the carbon yield when the C/CaO composite was washed with HCl. Note that it is difficult to determine the W_{carbon} through TG analysis of C/CaO because it is prone to hydration when exposed to air. W_{carbon} can be converted into the average stacking number of graphene layers (N_{stack}) by the following equation.

$$N_{stack} = \frac{W_M}{W_{graphene}} = \frac{W_{carbon}}{S_{template}\ W_{graphene}} \quad (1)$$

where W_M [g m^{-2}] is the average amount of carbon deposited on a unit surface area of the template, calculated by $W_M = W_{carbon}/S_{template}$. $S_{template}$ is the specific surface area of the template heated at the CVD temperature (850 or 900 °C). $S_{template}$ of SK2 heat-treated at 850 °C is 21 m^2 g^{-1}, while that heat-treated at 900 °C is 17 m^2 g^{-1}. $W_{graphene}$ is the weight of graphene per unit area (7.614 ×10^{-4} g m^{-2}).

The structures of the samples at each production step were observed by a scanning electron microscope (SEM; S-4800, Hitachi High-Tech Co., Ltd.). SK2, which was heat-treated at 850 °C, was observed by a scanning transmission electron microscope (STEM; FEI Company, Titan 80–300) for high-angle annular dark-field (HAADF) observation and energy dispersive X-ray spectroscopy (EDX). The crystallinity of CMS and GMS was characterized by XRD and by Raman spectroscopy on a Jasco NRS-3300FL spectrometer (excitation wavelength was 532.2 nm). The Raman shift was calibrated by the G-band position (1582 cm^{-1}) of highly oriented pyrolytic graphite (HOPG), and the intensity was normalized by the G-band (1582 cm^{-1}). The porous properties of CMS and GMS were characterized by N_2 adsorption-desorption measured at −196 °C. Total pore volume (V_{total}) was calculated at P/P_0 = 0.96. The

mesopore-size distribution was calculated by the Barrett-Joyner-Halenda (BJH) method applied to the adsorption isotherm. Advanced temperature-programmed desorption (TPD) analysis up to 1800 °C was conducted to estimate the number of edge sites. [44] The oxidation resistance was characterized by TG in air.

3. Results and discussion

3.1. The properties of CaO generated from $CaCO_3$

The gas emission during the $CaCO_3$ decomposition was analyzed by GC, as shown in Fig. 1a. Only CO_2 and H_2O were detected. The H_2O emission at relatively low temperatures is due to the desorption of physisorbed water. The intense CO_2 emission above 650 °C is ascribed to the $CaCO_3$-to-CaO conversion. The SK2-type $CaCO_3$ shows a slightly lower amount of CO_2 emission (9.2 mmol g^{-1}) compared to the stoichiometric amount of $CaCO_3$-to-CaO conversion (10.0 mmol g^{-1}), probably due to a low level of impurities included in SK2 (Table S1). The TG curves of $CaCO_3$ are shown in Fig. 1b. The SK2-type $CaCO_3$ shows an initial weight loss due to the desorption of physisorbed water, followed by successive weight losses. The total weight loss is 43.6 %, slightly lower than the stoichiometric value (44.0 %), as the GC result also indicated.

The XRD patterns of $CaCO_3$ before and after the heat treatments at 850 and 900 °C are shown in Fig. S1. As expected, the $CaCO_3$-to-CaO conversion is confirmed in both samples. The amount of impurities included in $CaCO_3$ (Table S1) is too small to be detected in the XRD patterns. The change of surface area by thermal decomposition of $CaCO_3$ was analyzed by the N_2 physisorption technique. Fig. 1c and S2 show N_2 adsorption-desorption isotherms of $CaCO_3$ before and after the thermal decomposition at 900 °C (the data after decomposition at 850 °C is shown in Fig. S3). The surface area of $CaCO_3$ noticeably decreases (from 78 to 17 m^2 g^{-1}), indicating thermal shrinkage. Next, we quantified the amounts of base and acid sites of CaO generated by the thermal decomposition of $CaCO_3$ using CO_2-TPD and NH_3-TPD, respectively, as shown in Fig. 1d. CaO shows intense CO_2 desorption around 575 °C, indicating the presence of base sites. The total CO_2 desorption amount, corresponding to the number of base sites, is 0.40 mmol g^{-1}. On the other hand, NH_3-TPD results indicate almost no acid sites. [45]

3.2. The reaction of methane on CaO

We had previously revealed that surface oxygen of γ-Al_2O_3 or MgO is eliminated as CO when the surface is encountered with CH_4 around 900 °C. [34] Then, the oxygen-vacancy sites catalyze the CH_4-to-C conversion reaction. [34] In this study, we have investigated the conversion of CH_4 using CaO produced through the thermal decomposition of SK2-type $CaCO_3$. Fig. 2 shows gas emission profiles during the CVD-GC analysis, together with the reference data on γ-Al_2O_3 and MgO. [34] In γ-Al_2O_3, the CO emission (Fig. 2a), which corresponds to the aforementioned reaction between surface oxygen and CH_4, gradually occurs from the beginning of CVD and continues up to 150 min. After the formation of the oxygen-vacancy sites, which activate the surface, the CH_4-to-C conversion reaction starts at around 50 min, as indicated by the H_2 emission (Fig. 2b). In MgO, much more intense CO emission occurs at the beginning of CVD (Fig. 2a), and the CH_4-to-C conversion reaction starts much earlier (at around 10 min), as found from Fig. 2b. These behaviors indicate that the O of MgO is eliminated more easily as CO than in γ-Al_2O_3, and the MgO surface is more active for the CH_4-to-C reaction. [34] For both γ-Al_2O_3 and MgO, the H_2 emission continues for more than 200 min without termination. [34] It is noteworthy that the behavior of CaO derived from SK2 is different from γ-Al_2O_3 and MgO. The initial CO emission from CaO is more intense than MgO. Interestingly, the order of CO desorption, a kind of redox reaction, is opposite to the bulk reduction reactions. In CaO, intense H_2 emission occurs very early, indicating a much faster rate of graphene growth compared to γ-Al_2O_3 and MgO. Significant reaction rates are important for the mass production of graphene sheets because they shorten the process time, enabling better production.

3.3. The effect of CVD conditions

From the results shown above, CaO generated from $CaCO_3$ (SK2) has high activity towards the CH_4-to-C reaction and is expected to play the role of a hard template for GMS production. Thus, we tried to determine the optimal CVD conditions (temperature and period) for which a high S_{BET} is achieved under 20 vol % CH_4/Ar feed. CMS is expected to have a high S_{BET} approaching 2627 m^2 g^{-1}, the value of single-layer graphene, when carbon coating is uniform and N_{stack} is close to 1. Additionally, the framework should be free from significant capillary shrinkage after template removal to retain the high S_{BET}. The CVD conditions and the resulting N_{stack} and S_{BET} of CMS are summarized in Table 1. Depending on the synthesis conditions, a series of materials with reasonably continuous properties can be produced, ensuring good reproducibility of the current process. The carbon recovery amount (Y_{carbon} [%]) upon the template removal, which is based on the C/CaO mass, and V_{total} are shown together. It is possible to roughly estimate the average graphene stacking number ($N_{stack\text{-}BET}$) of a porous carbon also by the following equation when the effect of carbon edge sites is negligible:

$$N_{stack-BET} = \frac{2627}{S_{BET}} \quad (2)$$

where 2627 (m^2 g^{-1}) is the specific surface area of single-layer graphene. While N_{stack} is the calculated value based on the structure of C/CaO, $N_{stack\text{-}BET}$ is calculated based on the structure of CMS after template removal. Thus, comparing N_{stack} and $N_{stack\text{-}BET}$ allows us to estimate the degree of structural change mainly caused by capillary shrinkage after template removal. If significant capillary shrinkage occurs, it causes re-stacking of graphene sheets, resulting in much larger $N_{stack\text{-}BET}$ than N_{stack}. On the other hand, N_{stack} is considerably larger than $N_{stack\text{-}BET}$ in

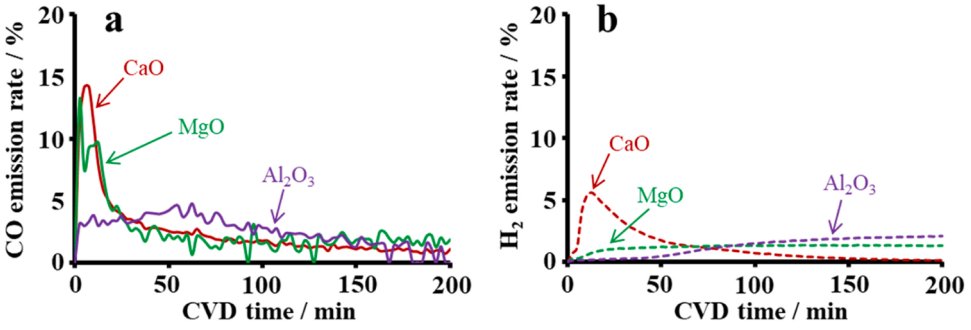

Fig. 2. The results of CVD-GC at 900 °C for (a) CO and (b) H_2 emissions. CH_4 supply was started at CVD time = 0. All the emission curves were normalized by dividing the data with the integrated amount during 200 min of the CVD time.

Entries 1–3, likely due to the significant formation of porous carbon structures from the presence of Mg-based impurities. It is found that Entries 5 and 6, which were performed at 850 °C for 1 h 20 min and 40 min, respectively, provide the best results: N_{stack} is 1.4, S_{BET} is larger than 1800 $m^2\ g^{-1}$, and $N_{stack\text{-}BET}$ is 1.4, which agrees well with N_{stack}, for both CVD conditions. In Entry 7, N_{stack} is equal to 1.2, but S_{BET} is slightly decreased compared to Entry 6. This indicates that N_{stack} of 1.4 is the best to avoid capillary shrinkage. When N_{stack} is decreased to 1.2, the mechanical strength of the carbon framework becomes compromised.

Thus, we conclude that the best CVD condition is Entry 6 (850 °C for 40 min). Note that Entry 5 and 6 yield similar results, but a shorter CVD time is more cost-effective for practical applications. The CMS prepared by this condition was further converted into GMS, as discussed in the next section. We previously reported that the optimum CVD conditions for γ-Al_2O_3 and MgO are 900 °C for 2 h and 900 °C for 50 min, respectively.[31,39] As shown in Fig. 2, CaO is more active for the CH_4-to-C conversion than γ-Al_2O_3 and MgO. Thus, the optimum CVD conditions for CaO are even milder than those for γ-Al_2O_3 and MgO.

3.4. The properties of CaO-derived GMS

GMS was synthesized from CMS obtained by Entry 6. A whole synthesis scheme is shown in Fig. 3a (route I), together with SEM images of each synthesis step (Fig. 3b-f). The CMS and GMS samples thus obtained are denoted as CMS(SK2-I) and GMS(SK2-I), respectively. As calculated from Fig. 1d and S3, the S_{BET} of SK2 decreases from 78 $m^2\ g^{-1}$ to 21 $m^2\ g^{-1}$ when heated at the CVD temperature of 850 °C. Thus, the average particle size calculated from S_{BET} increases from 28 nm to 86 nm (Fig. 3b and c). Also, numerous tiny particles (< 10 nm) are generated by thermal decomposition at 850 °C (Fig. 3c). These nanoparticles were further analyzed by HAADF-STEM and EDX, as shown in Fig. 4. HAADF-STEM image (Fig. 4a) displays that the tiny particles are attached to large particles with the size of about 100 nm, as shown in Fig. 3c. The Ca-EDX and O-EDX images (Fig. 4b and c) clearly indicate that the large particle is CaO. On the other hand, the Mg and O positions in Figs. 4c and d overlap well with the nanoparticles in Figs. 4a and e. Thus, we conclude that Mg (2 wt %) included in SK2 is deposited as tiny MgO particles (< 10 nm) by the thermal decomposition, as illustrated in Fig. 3a. Since both CaO and MgO catalyze the CH_4-to-C conversion (Fig. 2), their surfaces can be uniformly covered with a carbon layer. Indeed, the sample morphology remains unchanged before (Fig. 3c) and after (Fig. 3d) CVD. The carbon-loading amount of C/CaO is estimated as 2.2 wt %, so that the SK2 powder to turn dark gray during CVD. Fig. 3e shows the SEM image of CMS(SK2-I) after HCl treatment. Since the size of CaO is as large as 86 nm, the carbon layer deposited on the CaO shows wrinkles caused by capillary shrinkage. Nevertheless, $N_{stack\text{-}BET}$ of CMS(SK2-I) is the same as N_{stack}, indicating that the shrunk graphene layer forms a bellows-like structure without stacking each other.

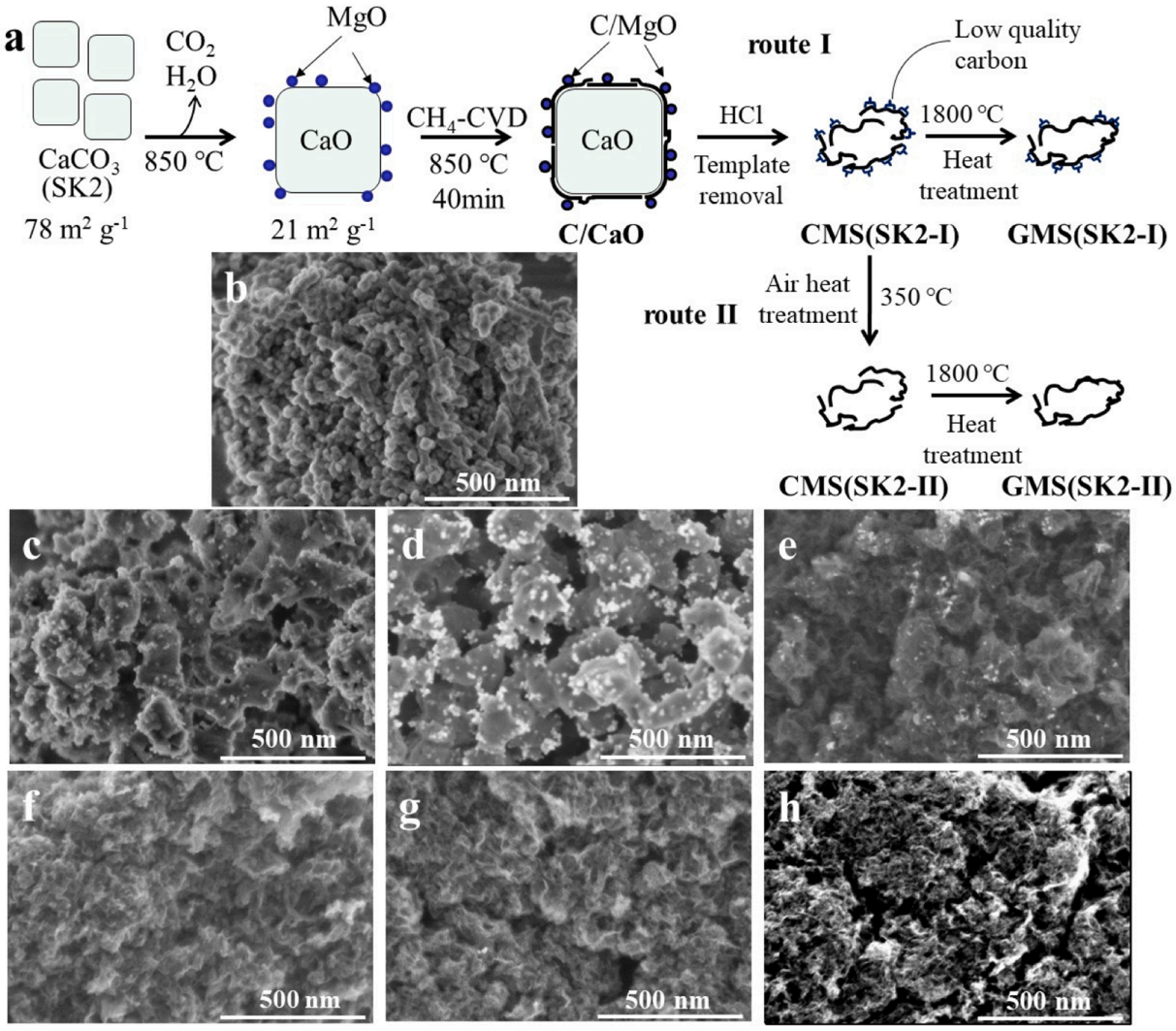

Fig. 3. (a) Schematic illustration of the synthesis process of GMS from $CaCO_3$ (SK2) by the procedure of Entry 6. (b–h) SEM images of (b) $CaCO_3$, (c) CaO formed by a heat-treatment of $CaCO_3$ at 850 °C, (d) C/CaO, (e) CMS(SK2-I), (f) GMS(SK2-I), (g) CMS(SK2-II), and (h) GMS(SK2-II).

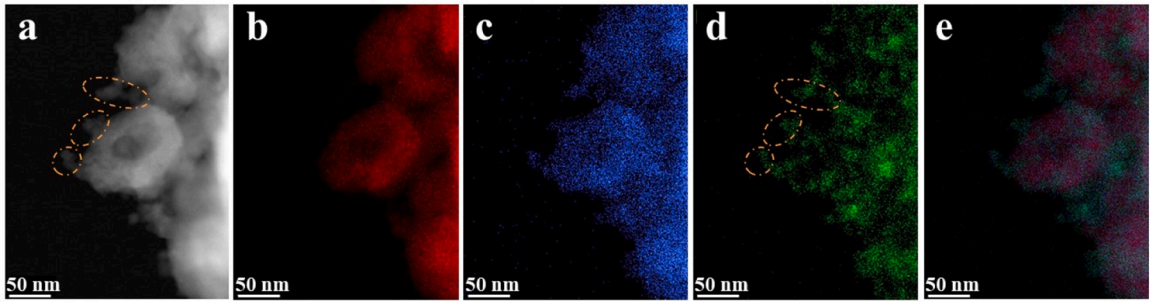

Fig. 4. (a) HAADF-STEM image and (b-e) EDX mapping images of $CaCO_3$ for (b) Ca, (c) O, (d) Mg, and (e) an overlay image of Ca+O+Mg. EDX images are taken at the same position as (a). The same positions of representative tiny particles are highlighted with dotted circles in (a) and (d).

Also, Fig. 3e shows dots corresponding to carbon deposited on the tiny MgO particles. When CMS(SK2-I) is turned into GMS(SK2-I) via heat treatment at 1800 °C, the wrinkled structure is not noticeably changed (Fig. 3f). On the other hand, the dots disappeared, indicating that these are thermally unstable carbon.

To examine the thermal stabilities of the two types of carbons in CMS (SK2-I), their oxidation behaviors were analyzed by TG in air, as shown in Fig. 5. The weight loss occurs stepwise: a small fraction (6.0 %) is burnt below 350 °C, and then the major component is burnt above 500 °C. To remove the former portion, which is ascribed to a low-crystallin carbon structure, CMS(SK2-I) was heat-treated at 350 °C in air. Such a purification technique is commonly used for carbon nanotubes. [46] The resulting CMS(SK2-II) shows only the wrinkled carbon framework (Fig. 3g). Thus, it is confirmed that the first slight weight loss (< 350 °C) in Fig. 5 corresponds to the oxidation of the dots found in Fig. 3e. Furthermore, CMS(SK2-II) was heat-treated at 1800 °C to prepare GMS (SK2-II) as shown in Fig. 3h.

Fig. 6a shows XRD patterns of CMS and GMS synthesized via routes I and II. CMS(SK2-I) has broad peaks of carbon 002 and 10, corresponding to graphene stacking and planar graphene structures, respectively. [47] Other small peaks are ascribed to inorganic impurities derived from the $CaCO_3$ sample (Table S1). When converted into GMS(SK2-I), both carbon 002 and 10 peaks become more intense, suggesting the development of graphene stacking structure and planar graphene structure. The XRD pattern of GMS(SK2-II) is very similar to that of GMS(SK2-I) because the amount of the low-crystalline carbon is only 6.0 wt % (Fig. 5).

The quality of graphene walls was further analyzed by Raman spectroscopy (Fig. 6b). The presence of the G-band in CMS and GMS samples indicates that these materials comprise graphene sheets. The G' band (also expressed as 2D band) can have a higher intensity than the G band in monolayer graphene [48,49] or few-layer graphenes with specific orientations. [50] Also, in monolayer and few-layer graphenes, the wavenumber of G' band is lower than that of G' band of graphite (2714 cm^{-1}). [26] The G' bands of both GMS samples satisfy the above conditions, suggesting that a large amount of monolayer or few-layer graphene is present in the GMS frameworks. The D and D′ bands correspond to defects that disrupt the symmetry of the hexagonal carbon rings in graphene. [30] There are two types of defects in graphene-based sp^2-carbon materials: edge sites and topological defects. The latter is non-hexagonal carbon rings in the graphene basal plane, including 5, 7, and 8-membered carbon rings. As will be discussed later, GMS possesses a minimal number of carbon edge sites. Consequently, an intense D band and a distinct D' band can be ascribed to the abundance of topological defects within the GMS framework. [26,30,35]

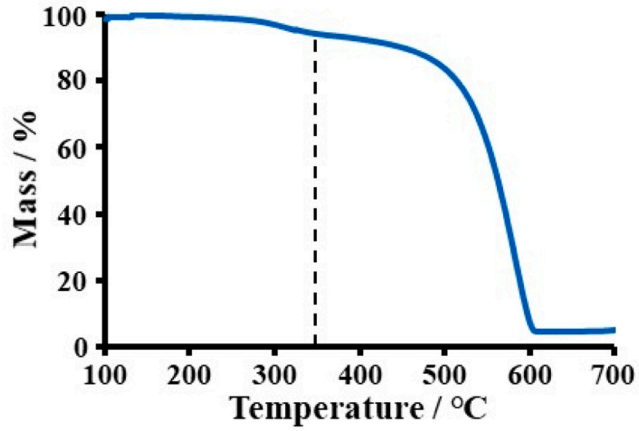

Fig. 5. TG curve of CMS(SK2-I) under air. The heating rate is 5 °C min^{-1}. The first weight loss ends at 350 °C, as indicated by a dotted line.

Fig. 6c shows N_2 adsorption-desorption isotherms of CMS and GMS. GMS(SK2-I) retains almost the same isotherm shape as that of CMS(SK2-I). As found from the mesopore-size distributions (Fig. 6d), GMS(SK2-I) retains the mesoporosity of the CMS(SK2-I) precursor, and such behavior is a unique feature for successful GMS synthesis. [26] Note that the porosity of GMS(SK2-II) is almost the same as that of GMS(SK2-I) because the amount of the low-crystalline carbon contained in CMS (SK2-I) is only 6.0 wt %. Despite the presence of small amounts of low-crystalline carbon in GMS(SK2-I), the physicochemical properties of GMS(SK2-I) and GMS(SK2-II) are indistinguishable by XRD, Raman spectroscopy, and N_2 physisorption. However, this does affect the amount of carbon edge sites in the corresponding GMSs, as shown in the next section.

3.5. Edge-free structure and oxidation resistance

A distinct advantage of GMS is the concomitant high porosity and negligible number of carbon edge sites. These seemingly conflicting properties enable GMS to behave as high-performance and highly durable electrode materials for supercapacitors, fuel cells, and secondary batteries. [28,30] To quantify the number of edge sites, we performed high-sensitivity vacuum TPD up to 1800 °C. [44] When a carbon material is heated, its edge sites terminated by H or O undergo decomposition, releasing H_2, CO, CO_2, and H_2O. The amount of carbon edge sites can be roughly estimated by the total gas emission amount (N_{gas}). It was observed that GMS(SK2-I) shows a considerable amount of gas emission (N_{gas} = 1.1 mmol g^{-1}) in comparison to the reported values for typical GMS (< 0.2 mmol g^{-1}). [26,34] A possibility is that the low-crystalline carbon was turned into not planar graphene walls but small carbon clusters having some dangling bonds, which can be easily oxidized when the sample was exposed to air after the 1800 °C treatment. Although the porosity of GMS(SK2-I) (S_{BET} = 1734 m^2 g^{-1}, V_{total} = 2.4 cm^3 g^{-1}) is satisfactory, it has many edge sites that cause corrosion in electrochemical applications. [51] We have produced CMS(SK2-II) through route II depicted in Fig. 3a, eliminating the presence of low-crystalline carbon, and subsequently transformed it into GMS(SK2-II). As we expected, GMS(SK-2-II) rarely shows gas emission (Fig. 7a), and its N_{gas} is as low as 0.16 mmol g^{-1}. Moreover, GMS(SK-2-II) possesses a

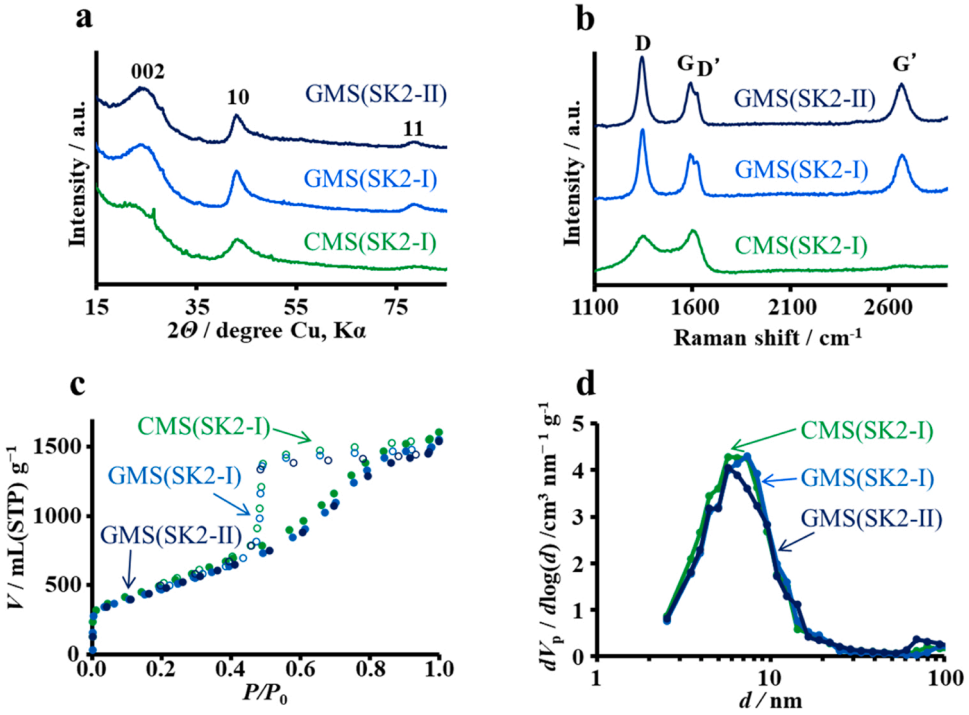

Fig. 6. The characterization results of CMS and GMS synthesized via routes I and II. (a) XRD patterns, (b) Raman spectra, (c) N_2 adsorption-desorption isotherms, and (d) Mesopore-size distributions.

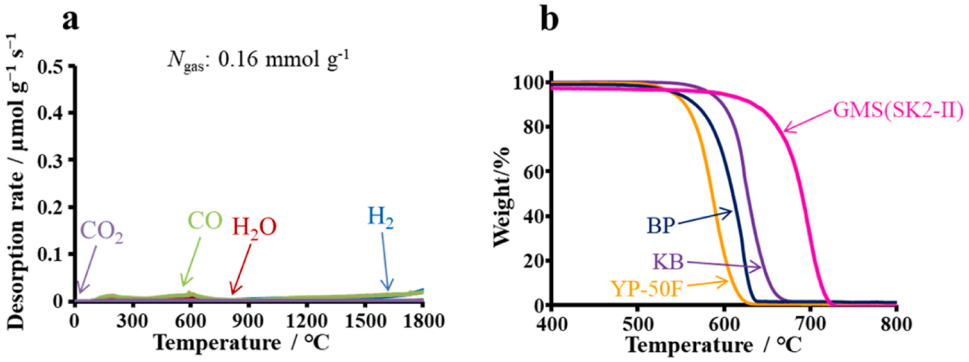

Fig. 7. Gas (H_2, H_2O, CO, and CO_2) evolution patterns of (a) GMS(SK2-II) during the high-sensitivity TPD measurement up to 1800 °C. The total gas emission amount (N_{gas}) is described. (b) Combustion TG curves. The heating rate is 5 °C min^{-1}. The data of reference carbon materials (activated carbon YP-50 F; carbon blacks BP, and KB) were taken from ref. [26,34].

developed porosity (1720 m^2 g^{-1}, 2.3 cm^3 g^{-1}). The small number of edge sites significantly enhances the oxidation resistance of carbon materials. [26,34]

Finally, the oxidation resistance of GMS(SK2-II) is compared with those of reference carbon materials by measuring combustion TG curves in Fig. 7b. As indicated in Fig. 7b, GMS(SK2-II) exhibits superior oxidation resistance compared to the reference carbon materials. The enhanced oxidation resistance of GMS(SK2-II) is attributed to the removal of the low-crystalline carbon.

The developed graphene domains (Fig. 6a and b), the abundance of topological defects (Figs. 6b and 7a), a low N_{gas} emission of 0.16 mmol g^{-1} (Fig. 7a), well-developed porosity (Fig. 6c and d), and high oxidation resistance (Fig. 7b) all demonstrate that high-quality GMS can be synthesized using the method reported in this work. We have previously documented that GMS possesses unique functions in various applications compared to conventional carbon materials such as graphite, carbon black, activated carbons, and carbon nanotubes, due to its specific structure. Its high surface area and edge-free structure make it suitable for fabricating supercapacitors with high-voltage stability. [28] The developed mesoporosity and edge-free structure also offer advantages as cathode materials for Li-O_2 batteries. [29,30] Furthermore, its edge-free and topological-defect-rich properties are crucial for serving as durable catalyst supports with an abundance of anchoring sites for catalysts. [27] In the current work, we do not present these performance data to avoid redundancy with our previous publications.

In the wet synthesis process of manufacturing $CaCO_3$ nanoparticles, [52] it is essential to add inorganic impurities to restrict particle growth, like the use of Mg in SK2. Although these impurities contribute to the formation of low-quality carbon moieties, we have demonstrated that it is possible to selectively remove these moieties through mild oxidation in air at 350 °C to obtain high-purity GMS materials. However, the multi-step procedure for GMS production may increase costs. Therefore, it would be desirable to establish a synthesis route capable of mass-producing $CaCO_3$ nanoparticles without inorganic impurities to eliminate the need for the removal process of low-quality carbon moieties in the future. Additionally, further reduction in the particle size of

the CaO template remains a challenge. As demonstrated in this work, the yield of carbon using CaO with a diameter of 86 nm is limited to 2–3 %, which is much lower than the yield of 12–14 % achieved with Al_2O_3 of approximately 7 nm. [26] Thus, decreasing the particle size of the template is crucial to increase the yield of carbon. Several methods exist for fabricating $CaCO_3$ nanoparticles in liquid [53] and gas phases, [54–56] and it is anticipated that new fabrication techniques will be developed in the future.

4. Conclusions

In this study, we utilized CaO generated from $CaCO_3$ nanoparticles as a solid template for synthesizing GMS. Initially, the $CaCO_3$ particles are 28 nm in size, which increase to 86 nm upon heating to 850 °C, transforming them into CaO. During this process, about 2 wt % of Mg, present as an inorganic impurity in $CaCO_3$, is converted into tiny MgO particles (< 10 nm). Applying CVD to the thermally decomposed product coats the CaO nanoparticles with a high-quality graphene layer, catalyzed distinctly by CaO, whereas the MgO particles result in the formation of low-quality carbon. After removing the template and subsequent high-temperature annealing at 1800 °C, GMS is produced. However, the presence of low-quality carbon significantly reduces the chemical stability of GMS. We have developed a remedy by treating the material in air at 350 °C, which effectively removes the detrimental low-crystalline carbons. This optimized synthesis process enables the production of high-quality GMS characterized by a minimal number of edge sites, evidenced by very low gas emission (0.16 mmol g^{-1}) during high-temperature TPD analysis. Additionally, the high-quality GMS exhibits well-developed porosity (1720 m^2 g^{-1} and 2.3 cm^3 g^{-1}), presenting promising opportunities for various applications.

CRediT authorship contribution statement

Shogo Sunahiro: Writing – original draft, Investigation, Formal analysis, Data curation. **Kritin Pirabul:** Data curation. **Zhengze Pan:** Investigation. **Takeharu Yoshii:** Investigation. **Yuichiro Hayasaka:** Investigation, Data curation. **Qi Zhao:** Investigation, Data curation. **Rachel Crespo-Otero:** Validation, Investigation. **Devis Di Tommaso:** Validation, Investigation. **Takashi Kyotani:** Writing – review & editing, Validation. **Hirotomo Nishihara:** Writing – review & editing, Validation, Supervision, Project administration, Methodology, Funding acquisition, Conceptualization.

Declaration of Competing Interest

The authors declare that they have no known competing financial interests or personal relationships that could have appeared to influence the work reported in this paper.

Data availability

Data will be made available on request.

Acknowledgments

This work was supported by JSPS KAKENHI Grant no. 23H00227; Council for Science, Technology and Innovation (CSTI), Cross-ministerial Strategic Innovation Promotion Program (SIP), the 3rd period of SIP "Creating a materials innovation ecosystem for industrialization" (Funding agency: NIMS); and UK's Royal Society International Exchanges Cost Share (IECR3193106). The authors thank Shiraishi Kogyo Co., Ltd., Sasol Ltd., for kindly supplying calcium carbonate nanoparticles and alumina nanoparticles, respectively. The authors acknowledge the kind support of Prof. H. Kato in performing Raman spectroscopy. Qi Zhao thanks the China Scholarship Council for financial support. Via our membership of the UK's HEC Materials Chemistry Consortium, which is funded by EPSRC (EP/L000202), this work used the ARCHER UK National Supercomputing Service (http://www.archer.ac.uk). We are grateful to the UK Materials and Molecular Modelling Hub for computational resources, which is partially funded by EPSRC (EP/P020194/1 and EP/T022213/1). This research utilized Queen Mary's Apocrita HPC facility, supported by QMUL Research-IT.

Appendix A. Supporting information

Supplementary data associated with this article can be found in the online version at doi:10.1016/j.cattod.2024.114763.

References

[1] J. Quílez-Bermejo, E. Morallón, D. Cazorla-Amorós, Metal-free heteroatom-doped carbon-based catalysts for ORR: a critical assessment about the role of heteroatoms, Carbon 165 (2020) 434–454.
[2] M.-M. Titirici, M. Antonietti, Chemistry and materials options of sustainable carbon materials made by hydrothermal carbonization, Chem. Soc. Rev. 39 (2010) 103–116.
[3] Z. Heidarinejad, M.H. Dehghani, M. Heidari, G. Javedan, I. Ali, M. Sillanpää, Methods for preparation and activation of activated carbon: a review, Environ. Chem. Lett. 18 (2020) 393–415.
[4] I. Ogino, Y. Suzuki, S.R. Mukai, Tuning the pore structure and surface properties of carbon-based acid catalysts for liquid-phase reactions, ACS Catal. 5 (2015) 4951–4958.
[5] T. Tsuchiya, T. Mori, S. Iwamura, I. Ogino, S.R. Mukai, Binderfree synthesis of high-surface-area carbon electrodes via CO_2 activation of resorcinol–formaldehyde carbon xerogel disks: analysis of activation process, Carbon 76 (2014) 240–249.
[6] H. Nishihara, T. Kyotani, Zeolite-templated carbons - three-dimensional microporous graphene frameworks, Chem. Commun. 54 (2018) 5648–5673.
[7] H. Nishihara, H. Fujimoto, H. Itoi, K. Nomura, H. Tanaka, M.T. Miyahara, P. A. Bonnaud, R. Miura, A. Suzuki, N. Miyamoto, N. Hatakeyama, A. Miyamoto, K. Ikeda, T. Otomo, T. Kyotani, Graphene-based ordered framework with a diverse range of carbon polygons formed in zeolite nanochannels, Carbon 129 (2018) 854–862.
[8] H. Nishihara, T. Kyotani, Templated nanocarbons for energy storage, Adv. Mater. 24 (2012) 4473–4498.
[9] H. Itoi, H. Nishihara, T. Kogure, T. Kyotani, Three-dimensionally arrayed and mutually connected 1.2-nm nanopores for high-performance electric double layer capacitor, J. Am. Chem. Soc. 133 (2011) 1165–1167.
[10] M.S. Ahmad, Y. Nishina, Graphene-based carbocatalysts for carbon–carbon bond formation, Nanoscale 12 (2020) 12210–12227.
[11] R.K. Joshi, S. Alwarappan, M. Yoshimura, V. Sahajwalla, Y. Nishina, Graphene oxide: the new membrane material, Appl. Mater. Today 1 (2015) 1–12.
[12] H. Nishihara, T. Hirota, K. Matsuura, M. Ohwada, N. Hoshino, T. Akutagawa, T. Higuchi, H. Jinnai, Y. Koseki, H. Kasai, Y. Matsuo, J. Maruyama, Y. Hayasaka, H. Konaka, Y. Yamada, S. Yamaguchi, K. Kamiya, T. Kamimura, H. Nobukuni, F. Tani, Synthesis of ordered carbonaceous frameworks from organic crystals, Nat. Commun. 8 (2017) 109.
[13] T. Ogoshi, Y. Sakatsume, K. Onishi, R. Tang, K. Takahashi, H. Nishihara, Y. Nishina, B.D.L. Campéon, T. Kakuta, T.-A. Yamagishi, The carbonization of aromatic molecules with three-dimensional structures affords carbon materials with controlled pore sizes at the Ångstrom-level, communications, Chemistry 4 (2021) 75.
[14] T. Yoshii, K. Chida, H. Nishihara, F. Tani, Ordered carbonaceous frameworks: a new class of carbon materials with molecular-level design, Chem. Commun. 58 (2022) 3578–3590.
[15] M.T. Gilbert, J.H. Knox, B. Kaur, Porous Glassy - Carbon, A new columns packing material for gas-chromatography and high-performance liquid-chromatography, Chromatographia 16 (1982) 138–148.
[16] R.W. Pekala, R.W. Hopper, Low-density microcellular carbon foams, J. Membr. Sci. 22 (1987) 1840–1844.
[17] T. Kyotani, L.-f Tsai, A. Tomita, Formation of ultrafine carbon tubes by using an anodic aluminum oxide film as a template, Chem. Mater. 7 (1995) 1427–1428.
[18] T. Kyotani, N. Sonobe, A. Tomita, Formation of highly orientated graphite from polyacrylonitrile by using a two-dimensional space between montmorillonite lamellae, Nature 331 (1988) 331–333.
[19] T. Kyotani, T. Nagai, S. Inoue, A. Tomita, Formation of new type of porous carbon by carbonization in zeolite nanochannels, Chem. Mater. 9 (1997) 609–615.
[20] A.A. Zakhidov, R.H. Baughman, Z. Iqbal, C.X. Cui, I. Khayrullin, S.O. Dantas, I. Marti, V.G. Ralchenko, Carbon structures with three-dimensional periodicity at optical wavelengths, Science 282 (1998) 897–901.
[21] R. Ryoo, S.H. Joo, S. Jun, Synthesis of highly ordered carbon molecular sieves via template-mediated structural transformation, J. Phys. Chem. B 103 (1999) 7743–7746.
[22] J. Lee, S. Yoon, T. Hyeon, S.M. Oh, K.B. Kim, Synthesis of a new mesoporous carbon and its application to electrochemical double-layer capacitors, Chem. Commun. (1999) 2177–2178.

[23] C.D. Liang, K.L. Hong, G.A. Guiochon, J.W. Mays, S. Dai, Synthesis of a large-scale highly ordered porous carbon film by self-assembly of block copolymers, Angew. Chem. Int. Ed. 43 (2004) 5785–5789.
[24] S. Tanaka, N. Nishiyama, Y. Egashira, K. Ueyama, Synthesis of ordered mesoporous carbons with channel structure from an organic-organic nanocomposite, Chem. Commun. (2005) 2125–2127.
[25] Y. Meng, D. Gu, F.Q. Zhang, Y.F. Shi, H.F. Yang, Z. Li, C.Z. Yu, B. Tu, D.Y. Zhao, Ordered mesoporous polymers and homologous carbon frameworks: amphiphilic surfactant templating and direct transformation, Angew. Chem. Int. Ed. 44 (2005) 7053–7059.
[26] H. Nishihara, T. Simura, S. Kobayashi, K. Nomura, R. Berenguer, M. Ito, M. Uchimura, H. Iden, K. Arihara, A. Ohma, Y. Hayasaka, T. Kyotani, Oxidation-resistant and elastic mesoporous carbon with single-layer graphene walls, Adv. Funct. Mater. 26 (2016) 6418–6427.
[27] A. Ohma, Y. Furuya, T. Mashio, M. Ito, K. Nomura, T. Nagao, H. Nishihara, H. Jinnai, T. Kyotani, Elucidation of oxygen reduction reaction and nanostructure of platinum-loaded graphene mesosponge for polymer electrolyte fuel cell electrocatalyst, Electrochim. Acta 370 (2021) 137705.
[28] K. Nomura, H. Nishihara, N. Kobayashi, T. Asada, T. Kyotani, 4.4 V supercapacitors based on super-stable mesoporous carbon sheet made of edge-free graphene walls, Energy Environ. Sci. 12 (2019) 1542–1549.
[29] W. Yu, Z. Shen, T. Yoshii, S. Iwamura, M. Ono, S. Matsuda, M. Aoki, T. Kondo, S. R. Mukai, S. Nakanishi, H. Nishihara, Hierarchically porous and minimally stacked graphene cathodes for high-performance lithium-oxygen batteries, Adv. Energy Mater. 14 (2024) 2303055.
[30] W. Yu, T. Yoshii, A. Aziz, R. Tang, Z.-Z. Pan, K. Inoue, M. Kotani, H. Tanaka, E. Scholtzová, D. Tunega, Y. Nishina, K. Nishioka, S. Nakanishi, Y. Zhou, O. Terasaki, H. Nishihara, Edge-site-free and topological-defect-rich carbon cathode for high-performance lithium-oxygen batteries, Adv. Sci. 10 (2023) 2300268.
[31] Z. Shen, W. Yu, A. Aziz, K. Chida, T. Yoshii, H. Nishihara, Sequential catalysis of defected-carbon and solid catalyst in Li–O2 batteries, J. Phys. Chem. C 127 (2023) 6239–6247.
[32] K. Nomura, H. Nishihara, M. Yamamoto, A. Gabe, M. Ito, M. Uchimura, Y. Nishina, H. Tanaka, M.T. Miyahara, T. Kyotani, Force-driven reversible liquid–gas phase transition mediated by elastic nanosponges, Nat. Commun. 10 (2019) 2559.
[33] G. Ning, Z. Fan, G. Wang, J. Gao, W. Qian, F. Wei, Gram-scale synthesis of nanomesh graphene with high surface area and its application in supercapacitor electrodes, Chem. Commun. 47 (2011) 5976–5978.
[34] S. Sunahiro, K. Nomura, S. Goto, K. Kanamaru, R. Tang, M. Yamamoto, T. Yoshii, J. N. Kondo, Q. Zhao, A. Ghulam Nabi, R. Crespo-Otero, D. Di Tommaso, T. Kyotani, H. Nishihara, Synthesis of graphene mesosponge via catalytic methane decomposition on magnesium oxide, J. Mater. Chem. A 9 (2021) 14296–14308.
[35] T. Xia, T. Yoshii, K. Nomura, K. Wakabayashi, Z.-Z. Pan, T. Ishii, H. Tanaka, T. Mashio, J. Miyawaki, T. Otomo, K. Ikeda, Y. Sato, M. Terauchi, T. Kyotani, H. Nishihara, Chemistry of zipping reactions in mesoporous carbon consisting of minimally stacked graphene layers, Chem. Sci. 14 (2023) 8448–8457.
[36] Q. Zhao, M. Yamamoto, K. Yamazaki, H. Nishihara, R. Crespo-Otero, D. Di Tommaso, The carbon chain growth during the onset of CVD graphene formation on γ-Al_2O_3 is promoted by unsaturated CH2 ends, Phys. Chem. Chem. Phys. 24 (2022) 23357–23366.
[37] B. Xu, L. Peng, G. Wang, G. Cao, F. Wu, Easy synthesis of mesoporous carbon using nano-CaCO3 as template, Carbon 48 (2010) 2377–2380.
[38] B. Xu, L. Shi, X.W. Guo, L. Peng, Z.X. Wang, S. Chen, G.P. Cao, F. Wu, Y.S. Yang, Nano-$CaCO_3$ templated mesoporous carbon as anode material for Li-ion batteries, Electrochim. Acta 56 (2011) 6464–6468.
[39] C. Zhao, W. Wang, Z. Yu, H. Zhang, A. Wang, Y. Yang, Nano-$CaCO_3$ as template for preparation of disordered large mesoporous carbon with hierarchical porosities, J. Mater. Chem. 20 (2010) 976–980.
[40] Y. Wen, X. Liu, X. Wen, X. Chen, K. Szymańska, R. Dobrzyńska, E. Mijowska, Na_3PO_4 assistant dispersion of nano-$CaCO_3$ template to enhance electrochemical interface: N/O/P co-doped porous carbon hybrids towards high-performance flexible supercapacitors, Compos. Part B Eng. 199 (2020) 108256.
[41] H. Wang, J. Wang, S. Xie, W. Liu, C. Niu, Template synthesis of graphitic hollow carbon nanoballs as supports for SnOx nanoparticles towards enhanced lithium storage performance, Nanoscale 10 (2018) 6159–6167.
[42] H. Gu, D. Cao, J. Wang, X. Lu, Z. Li, C. Niu, H. Wang, Micro-$CaCO_3$ conformal template synthesis of hierarchical porous carbon bricks: as a host for SnO_2 nanoparticles with superior lithium storage performance, materials today, Energy 4 (2017) 75–80.
[43] C. Tang, B.-Q. Li, Q. Zhang, L. Zhu, H.-F. Wang, J.-L. Shi, F. Wei, CaO-Templated growth of hierarchical porous graphene for high-power lithium-sulfur battery applications, Adv. Funct. Mater. 26 (2016) 577–585.
[44] T. Ishii, S. Kashihara, Y. Hoshikawa, J.-i Ozaki, N. Kannari, K. Takai, T. Enoki, T. Kyotani, A quantitative analysis of carbon edge sites and an estimation of graphene sheet size in high-temperature treated, non-porous carbons, Carbon 80 (2014) 135–145.
[45] M.V. Juskelis, J.P. Slanga, T.G. Roberie, A.W. Peters, A comparison of CaO, beta, and a dealuminated Y by ammonia TPD and by temperature programmed 2-propylamine cracking, J. Catal. 138 (1992) 391–394.
[46] K. Behler, S. Osswald, H. Ye, S. Dimovski, Y. Gogotsi, Effect of thermal treatment on the structure of multi-walled carbon nanotubes, J. Nanopart. Res. 8 (2006) 615–625.
[47] J. Biscoe, B.E. Warren, An X-ray study of carbon black, J. Appl. Phys. 13 (1942) 364–371.
[48] A.C. Ferrari, J.C. Meyer, V. Scardaci, C. Casiraghi, M. Lazzeri, F. Mauri, S. Piscanec, D. Jiang, K.S. Novoselov, S. Roth, A.K. Geim, Raman spectrum of graphene and graphene layers, Phys. Rev. Lett. 97 (2006) 187401.
[49] A. Gupta, G. Chen, P. Joshi, S. Tadigadapa, P.C. Eklund, Raman scattering from high-frequency phonons in supported n-graphene layer films, Nano Lett. 6 (2006) 2667–2673.
[50] A. Jorio, L.G. Cançado, Raman spectroscopy of twisted bilayer graphene, Solid State Commun. 175-176 (2013) 3–12.
[51] R. Tang, K. Taguchi, H. Nishihara, T. Ishii, E. Morallón, D. Cazorla-Amorós, T. Asada, N. Kobayashi, Y. Muramatsu, T. Kyotani, Insight into the origin of carbon corrosion in positive electrodes of supercapacitors, J. Mater. Chem. A 7 (2019) 7480–7488.
[52] M. Takasaki, Y. Kezuka, M. Tajika, Y. Oaki, H. Imai, Evolution of calcite nanocrystals through oriented attachment and fragmentation: multistep pathway involving bottom-up and break-down stages, ACS Omega 2 (2017) 8997–9001.
[53] M. Farhadi Khouzani, D.M. Chevrier, P. Güttlein, K. Hauser, P. Zhang, N. Hedin, D. Gebauer, Disordered amorphous calcium carbonate from direct precipitation, CrystEngComm 17 (2015) 4842–4849.
[54] L. Posavec, J.T.N. Knijnenburg, F.M. Hilty, F. Krumeich, S.E. Pratsinis, M. B. Zimmermann, Dissolution and storage stability of nanostructured calcium carbonates and phosphates for nutrition, J. Nanopart. Res. 18 (2016) 310.
[55] H. Lu, P.G. Smirniotis, F.O. Ernst, S.E. Pratsinis, Nanostructured Ca-based sorbents with high CO_2 uptake efficiency, Chem. Eng. Sci. 64 (2009) 1936–1943.
[56] M. Huber, W.J. Stark, S. Loher, M. Maciejewski, F. Krumeich, A. Baiker, Flame synthesis of calcium carbonate nanoparticles, Chem. Commun. (2005) 648–650.